Pergamon

*Int. J. Impact Engng*, Vol. 17, pp. 615-626, 1995

0734-743X/95 $9.50+0.00

# VALIDATION AND CALIBRATION OF A LATERAL CONFINEMENT MODEL FOR LONG-ROD PENETRATION AT ORDNANCE AND HIGH VELOCITIES

**Yehuda Partom[1] and David L. Littlefield[2]**
[1] Institute for Advanced Technology, The University of Texas at Austin, Austin, Texas
[2] Southwest Research Institute, San Antonio, Texas

**Summary**—In designing targets for laboratory long-rod penetration tests, the question of lateral confinement often arises, "How wide should the target be to exert enough confinement?" For ceramic targets, the problem is enhanced as ceramics are usually weak in tension and therefore have less self-confinement capability. At high velocities the problem is enhanced even more as the crater radius and the extent of the plastic zone around it are larger. Recently we used the quasistatic cavity expansion model to estimate the resistance of ceramic targets and its dependence on impact velocity [1]. We validated the model by comparing it to computer simulations in which we used the same strength model. Here we use the same approach to address the problem of lateral confinement.

We solved the quasistatic cavity expansion problem in a cylinder with a finite outside radius "b" at which $\sigma_r$ (b) = 0 ($\sigma_r$ = radial stress component). We did this for three cases: ceramic targets, metal targets, and ceramic targets confined in a metal casing. Generally, $\sigma_r$ (a) is a decreasing function of "a" ("a" = expanding cavity radius, and $\sigma_r$ (a) = the stress needed to continue opening the cavity). In the usual cavity expansion problem $b \rightarrow \infty$, $\sigma_r$ (a) = const., R = -$\sigma_r$ (a) (R = resistance to penetration). For finite "b" we estimate R by averaging $\sigma_r$ (a) over a range $o \leq a \leq a_r$ (where $a_r$, the upper bound of the range, is calibrated from computer simulations).

We ran 14 computer simulations with the CTH wavecode and used the results to calibrate $a_r$ for the different cases and to establish the overall validity of our approach.

We show that generally for $D_t/D_p > 30$, the degree of confinement is higher than 95% ($D_t$ = target diameter; $D_p$ = projectile diameter; and degree of confinement = $R/R_\infty$; $R_\infty$ = resistance of a laterally infinite target). We also show that tensile strength of ceramic targets (represented by the spall strength $P_{min}$) has a significant effect on the degree of confinement, while other material parameters have only a minor effect.

## INTRODUCTION

We have recently developed a model to estimate the reduction of target resistance to long rod penetration that results from partial lateral confinement [2, 3]. The model is based on the quasistatic cylindrical cavity expansion model [4], and can handle metals and ceramics, as well as ceramics confined in a metal casing. Solving the cavity expansion model for a laterally finite target we get generally that:

$$\sigma_r = \sigma_r(a) \ , \tag{1}$$

where "a" is the radius of a cylindrical cavity opened from zero radius and $\sigma_r$ is the radial stress on the cavity boundary needed to continue opening it. We then assume that R is some average of $\sigma_r$ (a) over some range of "a."

$$R = \langle -\sigma_r(a) \rangle \qquad 0 < a < a_r \ . \tag{2}$$

In [2, 3] we use $a_r = a_c$ where $a_c$ is the penetration crater radius, and we average according to the plastic work. We use:

$$R = \frac{-\int_0^{a_c} \sigma_r(a)\, da}{\frac{1}{2} a_c^2} \quad . \tag{3}$$

This averaging scheme gives higher "a" values a larger weight, and as $\sigma_r(a)$ decreases with "a," the resulting reduction in R is quite large. The examples given in [2, 3] show a relatively large reduction in R for moderately unconfined targets.

To check the model as a whole, and the averaging scheme in particular, we ran a series of computer simulations with the CTH wave code [5]. From the simulation results we extract R values, assuming Tate's model, and compare them to the model predictions. We show that the averaging scheme adopted in [2, 3], and given by (3), is indeed overestimating the lateral effect. We therefore modify the averaging scheme and calibrate the averaging range from the simulation results. First, we describe the simulations and outline the results obtained from them. Next, we outline the main results obtained from the cavity expansion analysis in [2] and [3]. Next, we compare the model predictions to simulation results and calibrate the range of integration for ceramic (alumina AD995) and steel targets. After that, we employ the (calibrated) model to do a short parameter study, and we conclude with a summary of the main results and conclusions.

## SIMULATIONS

Simulations were done with the 2D CTH code [5] in the same way as in [1, 6]. In all runs but two, the projectile is a L/D = 10 tungsten alloy rod with D = 7.87 mm. In two runs, L/D = 20. For the target there are three cases: 1) alumina AD995; 2) RHA steel; and 3) alumina AD955 encased laterally in RHA steel.

The target has a depth of 250 mm and a diameter of 220 mm or less. In both the projectile and target, in regions where most of the "action" takes place, we use 0.787 x 0.787 mm cells. Beyond that, target cells grow gradually by a factor of 1.022 in the radial direction, and 1.018 in longitudinal direction. All boundaries are stress free.

The equations of state for the projectile and target materials are those used routinely at SwRI. For the projectile $\rho_p$ = 17.3 g/cc, and the constant flow stress is 2 GPa. For RHA steel $\rho_t$ = 7.85 g/cc, the shear modulus G = 80 GPa, and the constant flow stress is 1 GPa. For the alumina $\rho_t$ = 3.96 g/cc; G = 152 GPa and the strength model is the same as in [1, 6] with $Y_0$ = 1.5 GPa; $\alpha_1 = \alpha_2$ = 0.5; $P_1 = P_2$ = 10 GPa ($Y_1$ = 6.5 GPa, $Y_2$ = 5 GPa); and $P_{min}$ = -0.5 or -0.2 GPa. Strength model parameters are defined in Fig. 1 taken from [1].

Some of the parameters used for alumina AD995 are not those calibrated from planar impact tests and outlined in [7]. A better set of parameters for AD995 would be: $\rho_t$ = 3.89 g/cc; $Y_0$ = 3 GPa; $\alpha_1 = \alpha_2$ = 1; $Y_1$ = 6 GPa; and $Y_2$ = 5.5 GPa. Not using the right parameters does not impair the validation process of our model as long as we use the same parameters in both the model and the simulation. At the most, we may need to adjust somewhat the averaging range calibrated from the simulations. The simulation runs are outlined in Table 1.

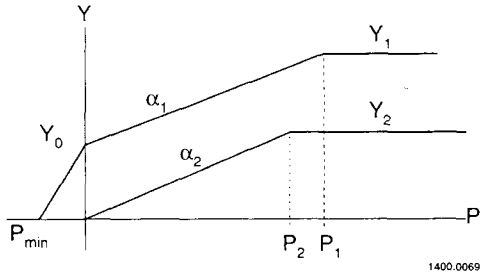


**Fig. 1. Schematic strength model for ceramics [1, 6]. Upper curve is the fracture surface for the intact material. Lower curve is the yield surface for the fractured (granular-like material). When the state point reaches the upper curve it drops instantaneously to the lower curve at the same pressure.**

**Table 1. List of the Simulation Runs**

| Case | Run No. | V km/s | $D_t$ ($D_c$ or $D_s$) mm | Δs mm | $P_{min}$ GPa | L/D |
|---|---|---|---|---|---|---|
| 1 | DOP 37 | 1.5 | 220 | 0 | -0.5 | 10 |
| 1 | 38 | 2.5 | 220 | 0 | -0.5 | 10 |
| 1 | 40 | 1.5 | 150 | 0 | -0.5 | 10 |
| 1 | 41 | 1.5 | 100 | 0 | -0.5 | 10 |
| 1 | 42 | 1.5 | 60 | 0 | -0.5 | 10 |
| 1 | 43 | 2.5 | 100 | 0 | -0.5 | 10 |
| 1 | 44 | 1.5 | 100 | 0 | -0.2 | 10 |
| 1 | 47 | 1.5 | 100 | 0 | -0.5 | 20 |
| 1 | 49 | 1.5 | 220 | 0 | -0.5 | 20 |
| 2 | TS 152 | 1.5 | 220 | NA | NA | 10 |
| 2 | 153 | 1.5 | 100 | NA | NA | 10 |
| 2 | 154 | 1.5 | 60 | NA | NA | 10 |
| 3 | DOP 45 | 1.5 | 60 | 5 | -0.5 | 10 |
| 3 | 46 | 1.5 | 60 | 10 | -0.5 | 10 |
| 3 | DOP 46 | 1.5 | 60 | 10 | -0.5 | 10 |

As in [1], we present the simulation results by penetration-erosion (pL) plots (Figs. 2 to 7). As in [1], we take the slopes (S) of these curves, just beyond the entrance boundary influence range, and use them to compute the target resistance (R) in the Tate model sense. The equation for that, as outlined in [1] is:

$$R = Y_p + \tfrac{1}{2}\rho_p V^2 f \quad , \tag{4}$$

$$f = \frac{1 - (S/S_h)^2}{(1+S)^2} \quad , \tag{5}$$

$$S_h^2 = \rho_p / \rho_t \quad . \tag{6}$$

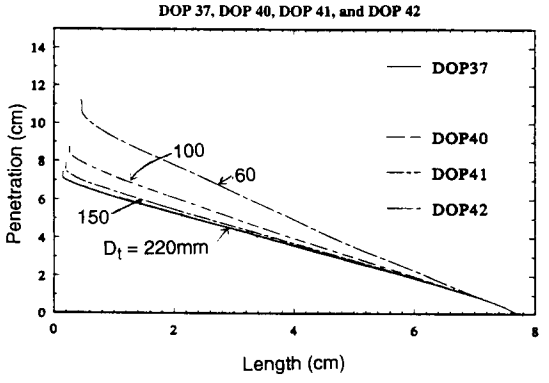


**Fig. 2. Ceramic target, effect of target diameter. Note that in Figs. 2 to 7, the axes are in cm (and not in mm).**

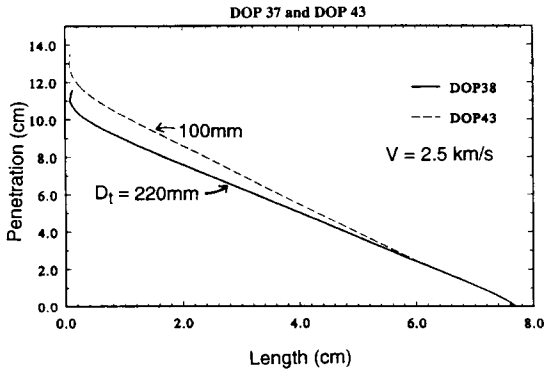


**Fig. 3. Ceramic target, V = 2.5 km/s, effect of target diameter at a higher velocity.**

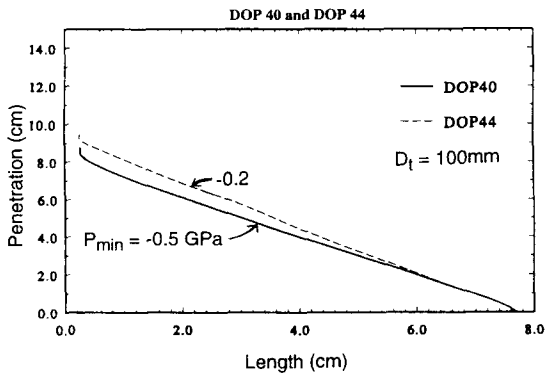


**Fig. 4. Ceramic target, $D_t$ = 100 mm, effect of tensile strength.**

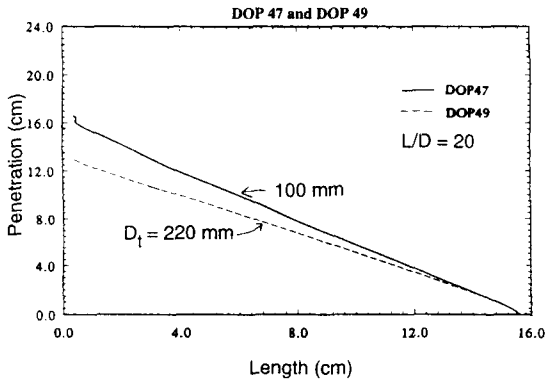


**Fig. 5. Ceramic target, L/D = 20, effect of higher L/D.**

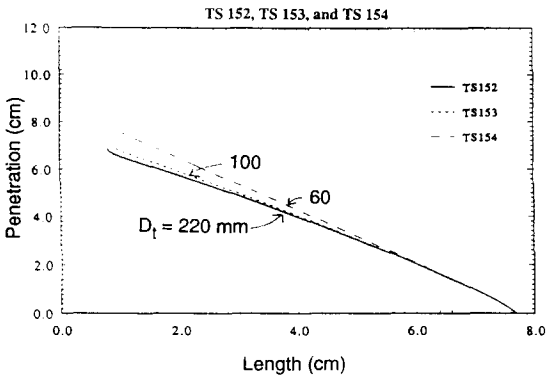


**Fig. 6. Steel target, effect of target diameter.**

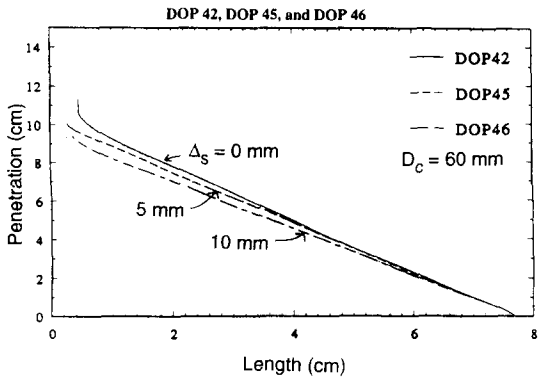


**Fig. 7. Ceramic confined by steel, effect of confinement thickness.**

The results obtained are given in Table 2, where we used:

$\rho_p / \rho_t = 4.37$ for the ceramic target

$\rho_p / \rho_t = 2.204$ for the steel target

$\frac{1}{2}\rho_p V^2 = 19.46$ GPa for V = 1.5 km/s

$\frac{1}{2}\rho_p V^2 = 54.06$ GPa for V = 2.5 km/s

$Y_p = 2$ GPa

From the results in Table 2 we draw the following conclusions:

- Comparing the results from Fig. 3 to those of Fig. 2, we see that at higher impact velocities resistance decreases more for the same decrease in confinement. Our confinement model does not include a dependence of resistance on velocity. To account for the velocity dependence, we calibrate the averaging range as a function of velocity.

- From the results in Fig. 4, we see the dependence of confinement on the tensile strength of the ceramic. This dependence is accounted for by our confinement model as discussed above.
- Comparing the results from Fig. 5 to those of Fig. 2, we see that the lateral confinement effect does not depend on the aspect ratio (L/D) of the projectile. (As seen from Fig. 5, the L/D = 20 runs were with the same diameter and a double length.)
- Comparing the results for steel targets (Fig. 6) to those of ceramic targets (Fig. 2), we see that the reduction of resistance in the ceramic is about twice as high.
- Finally, we see from Fig. 7 that confining the ceramic target in a steel casing does not significantly compensate for an undersize target. For $2\Delta s = 33\%\ D_c$ (where $D_c$ is the diameter of the ceramic) the increase in R is only about 10%.

**Table 2. Resistance Values (R) Extracted from the Simulation Results**

| | | | | | |
|---|---|---|---|---|---|
| **Case 1—from Fig. 2** | | | | | |
| **No.** | **$D_t$ (mm)** | **S** | **f** | **R (GPa)** | **$R/R_{220}$** |
| 37 | 220 | 0.875 | 0.2346 | 6.566 | 1.0 |
| 40 | 150 | 0.920 | 0.2187 | 6.256 | 0.9531 |
| | 100 | 1.013 | 0.1888 | 5.675 | 0.864 |
| 42 | 60 | 1.312 | 0.1134 | 4.207 | 0.641 |
| **Case 1—from Fig. 3** | | | | | |
| **No.** | **$D_t$ (mm)** | **S** | **f** | **R (GPa)** | **$R/R_{220}$** |
| 38 | 220 | 1.291 | 0.1179 | 8.374 | |
| 43 | 100 | 1.509 | 0.0761 | 6.113 | 0.730 |
| **Case 1—from Fig. 4** | | | | | |
| **No.** | **$P_{min}$ (GPa)** | **S** | **f** | **R (GPa)** | **$R/R_{220}$** |
| 41 | -0.5 | 1.013 | 0.1888 | 5.675 | |
| 44 | -0.2 | 1.174 | 0.1449 | 4.819 | 0.734 |
| **Case 1—from Fig. 5** | | | | | |
| **No.** | **$D_t$ (mm)** | **S** | **f** | **R (GPa)** | **$R/R_{220}$** |
| 49 | 220 | 0.831 | 0.2511 | 6.887 | |
| 47 | 100 | 0.969 | 0.2025 | 5.941 | 0.863 |
| **Case 2—from Fig. 6** | | | | | |
| **No.** | **$D_t$ (mm)** | **S** | **f** | **R (GPa)** | **$R/R_{220}$** |
| 152 | 220 | 0.956 | 0.1530 | 4.977 | |
| 153 | 100 | 1.006 | 0.1344 | 4.615 | 0.927 |
| 154 | 60 | 1.107 | 0.1000 | 3.946 | 0.793 |
| **Case 3—from Fig. 7** | | | | | |
| **No.** | **$\Delta s$ (mm)** | **S** | **f** | **R (GPa)** | **$R/R_{220}$** |
| 42 | 0 | 1.312 | 0.1134 | 4.207 | 0.641 |
| 45 | 5 | 1.290 | 0.1181 | 4.298 | 0.655 |
| 46 | 10 | 1.221 | 0.1136 | 4.599 | 0.700 |

Focusing on the initial parts of the curves in Figs. 2 to 7, we can make an additional important observation. We see that the different curves in each of the figures are initially on top of each other, and they start to separate only after some penetration (or some time). In Fig. 2, for example, the $D_t = 60$ mm curve deviates at L = 70 mm; the $D_t = 100$ mm curve at L = 65 mm; and the $D_t = 150$ mm curve at L = 58 mm. This means that the penetrating projectile "feels" the free lateral boundary only after some delay which is larger for wider targets. This may be the reason why poorly confined targets often display an initially high resistance.

## CONFINEMENT MODEL

Our confinement model is described in detail in [2] and [3]. We use the approach of the quasistatic cavity expansion [4] in cylindrical geometry, and apply it to the case of a free stress outer boundary. In the original cavity expansion model the outer boundary is at infinity. The results obtained for unencased alumina and RHA (Cases 1 and 2) are as follows:

*Case 1. Ceramic Target*

As long as $c < b + u(b) = b'$ we have:

$$\sigma_r(a) = -\sigma_r(c)\left(\frac{c^2}{a^2}\right)^{\gamma} , \tag{7}$$

$$\sigma_r(c) = \frac{-\beta Y_o\left(1-\frac{c^2}{b^2}\right)}{1-\frac{\xi c^2}{b^2}} , \tag{8}$$

$$\xi = \frac{2}{3}\beta\frac{Y_o}{P_{min}}(1+\nu) , \tag{9}$$

$$\frac{c^2}{a^2} = \frac{\frac{G}{\beta Y_o}\left(1-\frac{\xi c^2}{b^2}\right)}{1+(1-2\nu)\frac{c^2}{b^2}} , \tag{10}$$

$$\gamma = \frac{\alpha_2\beta}{1+\alpha_2\beta} \text{ where } \beta = \frac{\sqrt{3}}{3} , \tag{11}$$

$$R_\infty = \beta Y_o\left(\frac{G}{\beta Y_o}\right)^{\gamma} , \tag{12}$$

where:

a = radius of expanding cavity (starting from zero)
b = radius of outside (free) boundary
c = radius of elastic-plastic interface
u = radial displacement
$\sigma_r$ = radial stress
G = shear modulus
$\nu$ = Poisson's ratio
$Y_o$, $\alpha_2$, $P_{min}$ = strength parameters defined in Fig. 1

When $c = b'$ (elastic-plastic interface has reached the outside boundary) there is no resistance to further cavity expansion and,

$$\sigma_r(a) = 0 \quad ; \quad c = b + u(b) = b' . \tag{13}$$

*Case 2. Steel Target (Constant Y)*

As long as $c < b+u(b) = b'$, we have:

$$\sigma_r(a) = -\beta Y\left(1-\frac{c^2}{b^2}+\ln\frac{c^2}{a^2}\right) , \tag{14}$$

$$\frac{c^2}{a^2} = \frac{G}{\beta Y} \frac{1}{1-(1-2\nu)\frac{c^2}{b^2}} \quad , \tag{15}$$

$$R_\infty = \beta Y_o \left(\frac{G}{\beta Y_o}\right)^\gamma \quad . \tag{16}$$

When c = b+u (b) = b′ (elastic-plastic interface has reached the outside boundary), we have:

$$\sigma_r\,(a) = -\beta Y \ln\left(1 + \frac{b^2}{a^2}\right) \quad . \tag{17}$$

*Case 3. Ceramic Encased in Steel*

As long as c ≤ b+u (b) = b′ (elastic-plastic interface is in the ceramic, b = ceramic-steel interface radius), we have:

$$\sigma_r\,(a) = \sigma_r\,(c)\left(\frac{c^2}{a^2}\right)^\gamma \quad , \tag{18}$$

$$\sigma_r\,(c) = -\beta Y_o \frac{1 - \frac{M_3}{1-2\nu_c}\frac{c^2}{b^2}}{1 - M_4\frac{c^2}{b^2}} \quad , \tag{19}$$

$$\frac{c^2}{a^2} = \frac{G_c}{\beta Y_o} \frac{1 - M_4\frac{c^2}{b^2}}{1 + M_3\frac{c^2}{b^2}} \quad , \tag{20}$$

$$M_3 = \frac{2G_cM_1 + bM_2}{2(\lambda_c + G_c)M_1 - bM_2} \quad , \tag{21}$$

$$M_4 = \frac{\beta Y_o}{P_{min}} \frac{K_c}{G_c} M_3 \quad , \tag{22}$$

$$M_1 = \frac{b}{d^2}\left(1 - 2\nu_m + \frac{d^2}{b^2}\right) \quad , \tag{23}$$

$$M_2 = \frac{2G_m}{d^2}\left(1 - \frac{d^2}{b^2}\right) \quad , \tag{24}$$

where: d = outside radius of the steel casing; $\lambda_c$, $G_c$, $\nu_c$ = Lame modulus, shear modulus and Poisson's ratio of the ceramic; and $G_m$, $\nu_m$ = Shear modulus and Poisson's ratio of the steel.

When b′ < c < d + u (d) = d′ (elastic-plastic interface is in the steel):

$$\sigma_r(a) = \sigma_r(b')\left(\frac{b'^2}{a^2}\right)^\gamma \quad , \tag{25}$$

$$\sigma_r(b') = \sigma_r(c) - \beta Y_m \ln\frac{c^2}{b'^2} \quad , \tag{26}$$

$$\sigma_r(c) = -\beta Y_m\left(1 - \frac{c^2}{d^2}\right) \quad , \tag{27}$$

$$\frac{b'^2}{a^2} = 1 + \frac{b^2}{a^2} \quad , \tag{28}$$

$$\frac{c^2}{b'^2} = \frac{a^2}{a^2 + b^2}\frac{c^2}{a^2} \quad , \tag{29}$$

$$\frac{c^2}{a^2} = \frac{G_m}{\beta Y_m}\frac{1}{1 - (1-2\nu)c^2/d^2} \quad , \tag{30}$$

where: $Y_m$ = (constant) flow stress of the steel.

When c = d′ (elastic-plastic interface has reached the outside boundary), $\sigma_r$ (a) is still given by (25) and $b'^2/a^2$ by (28), but $\sigma_r$ (b′) is given by:

$$\sigma_r(b') = -\beta Y_m \ln \frac{d'^2}{b'^2} \quad , \tag{31}$$

$$\frac{d'^2}{b'^2} = \frac{a^2 + d^2}{a^2 + b^2} \quad . \tag{32}$$

When the elastic-plastic interface crosses the ceramic steel boundary, the cavity radius ($a_b$) is given approximately by:

$$a_b = b\left(\frac{\beta Y_o}{G_c}\frac{1 + M_3}{1 - M_4}\right)^{1/2} \quad . \tag{33}$$

When the elastic-plastic interface just reaches the outside boundary, the cavity radius ($a_d$) is given approximately by:

$$a_d = d\left(2\frac{\beta Y_m}{G_m}(1 - \nu_m)\right)^{1/2} \quad . \tag{34}$$

We see from the equations that in all three cases we get $\sigma_r$ (a) ≠ const., and it can be verified that $\sigma_r$(a) is a decreasing function of "a." As mentioned above, the resistance R is therefore obtained by averaging , $\sigma_r$ (a), as defined in (2).

Also, in deriving the expressions for $\sigma_r$ (a) we do not account for the dynamic pressure effect. The dynamic pressure effect on the resistance of ceramic targets is discussed in detail in [6] and [7]. We didn't include this effect in our confinement model because it would make the analysis intractable, and because we have assumed that its influence on the ratio $R/R_\infty$ would be small. We, therefore, anticipate that the averaging range (calibrated from the simulation) would come out to be somewhat impact velocity dependent.

## VALIDATION AND CALIBRATION OF THE CONFINEMENT MODEL

From preliminary comparisons, we concluded that the first moment averaging used in (3) over-emphasizes larger values of a. We therefore switched to simple averaging given by:

$$R = \frac{1}{a_r}\int_o^{a_r} -\sigma_r(a)\, da \quad , \tag{35}$$

where the averaging range $a_r$ is given by:

$$a_r = \frac{1}{2} e\, D_p \quad , \tag{36}$$

and e is calibrated from the simulation results. The procedure for validating and calibrating values of e is as follows:

- Calibrate an approximate e value (for each of the different cases).

- Obtain from the model values for $R_{220}/R_\infty$ using those e values. These ratios are close to 1 and are not sensitive to errors in e.
- Correct the values of $R_{220}/R_\infty$ in Table 2 to $R/R_\infty$ by:

$$R/R_\infty = (R/R_{220})\,(R_{220}/R_\infty) \tag{37}$$

- Plot curves of $R/R_\infty$ versus $D_t / D_p$ for different values of e, and superimpose on them the values of $R/R_\infty$ from the simulations. In this way, the model can be validated and e calibrated.

Values of $R/R_\infty$ obtained in this way from $R/R_{220}$ values in Table 2 are given in Table 3.

**Table 3. Relative Resistance Values from the Simulations**

| | | |
|---|---|---|
| **Case 1—from Fig. 8** | | |
| **No.** | **$R/R_{220}$** | **$R/R_\infty$** |
| 37 | 1.0 | 0.966 |
| 40 | 0.953 | 0.921 |
| 41 | 0.864 | 0.835 |
| 42 | 0.641 | 0.620 |
| **Case 1—from Fig. 9** | | |
| **No.** | **$R/R_{220}$** | **$R/R_\infty$** |
| 38 | 1.0 | 0.921 |
| 43 | 0.730 | 0.672 |
| **Case 1—from Fig. 10** | | |
| **No.** | **$R/R_{220}$** | **$R/R_\infty$** |
| 41 | 0.864 | 0.835 |
| 44 | 0.736 | 0.710 |
| **Case 1—from Fig. 11** | | |
| **No.** | **$R/R_{220}$** | **$R/R_\infty$** |
| 49 | 1.0 | 0.966 |
| 47 | 0.863 | 0.834 |
| **Case 2—from Fig. 12** | | |
| **No.** | **$R/R_{220}$** | **$R/R_\infty$** |
| 152 | 1.0 | 0.971 |
| 153 | 0.927 | 0.900 |
| 154 | 0.793 | 0.770 |
| **Case 3—from Fig. 13** | | |
| **No.** | **$R/R_{220}$** | **$R/R_\infty$** |
| 42 | 0.641 | 0.620 |
| 45 | 0.655 | 0.633 |
| 46 | 0.700 | 0.678 |

Values of $R/R_\infty$ from Table 3 are superimposed on curves from the confinement model in Figs. 8 to 13. Figs. 8 to 13 correspond to Figs. 2 to 7. Fig. 11 is missing because, as can be seen from Tables 2 and 3, $R/R_\infty$ is independent of L/D. Fig. 11 would look the same as Fig. 8. Fig. 8 is for ceramic targets at 1.5 km/s impact velocity. We see that $e = 0.47 \pm 0.02$ would fit the simulation results. Also, above $D_t/D_p = 25$ we get $R/R_\infty > 0.95$.

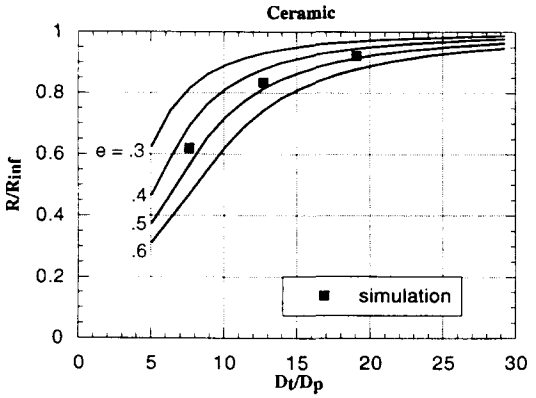


Fig. 8. Relative resistance ($R/R_\infty$) versus target to projectile diameter ratio ($D_t/D_p$). Curves are from confinement model. Different curves for different averaging range (½ e $D_p$). Black squares from simulation (Table 3). Ceramic (AD995 alumina) target. From the simulation, e ≅ 0.47.

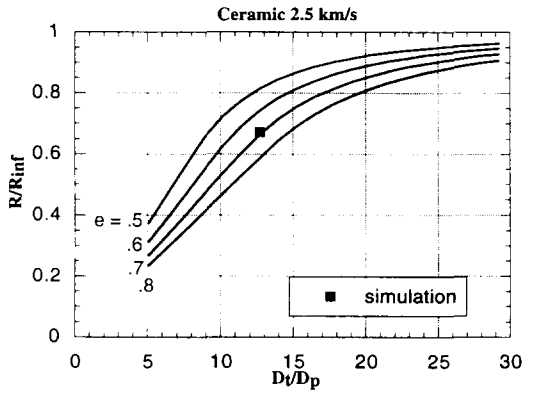


Fig. 9. Same as in Fig. 8, but at a higher impact velocity (2.5 km/s) instead of 1.5 km/s. From the simulation, e ≅ 0.7.

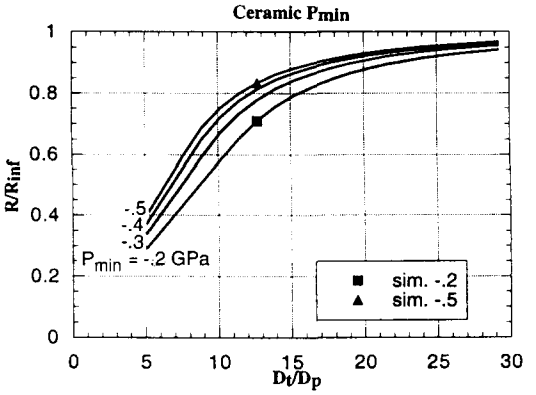


Fig. 10. Same as in Fig. 8 except that the different curves are for different values of $P_{min}$, and e ≅ 0.47.

Fig. 11. This figure has been omitted because it is the same as Fig. 8. As can be seen from Tables 2 and 3, $R/R_\infty$ is independent of L/D.

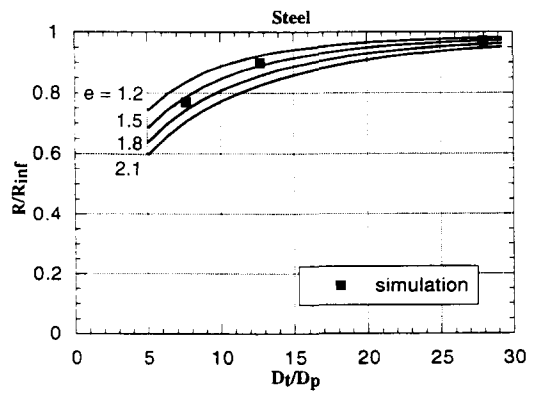


Fig. 12. Same as in Fig. 8 but for steel targets. From the simulation, e ≅ 1.5.

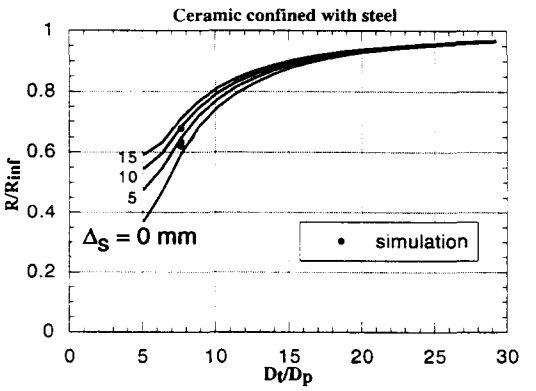


Fig. 13. Same as in Fig. 8 except that e = 0.47, and the different curves are for different thickness of steel casing.

Fig. 9 checks the influence of impact velocity on the degree of confinement in ceramic targets. We see that a higher value of e is needed. At 2.5 km/s, e ≅ 0.7. We also see that at $D_t$ / $D_p$ = 25, $R/R_\infty \cong 0.90$. This shows that as impact velocity increases, a lower degree of confinement is obtained for the same diameter ratio.

Fig. 10 checks the influence of the tensile strength of the ceramic represented by $P_{min}$. The curves are computed with e = 0.47 and we see that agreement with the simulation for $P_{min}$ = -0.2 GPa is good. We also see that the degree of confinement is quite sensitive to changes in tensile strength.

Fig. 12 is for steel targets. We see that a much higher value of e is needed, e = 1.55 ± 0.15. Also, at the same diameter ratios, steel targets are better confined than ceramic targets. This would justify encasing a ceramic target in steel.

Fig. 13 is for ceramic targets encased in steel. The different curves are for different values of steel thickness. We see that the casing significantly effects the degree of confinement only below $D_t/D_p$ = 15. But at the same time, we may have the plastic zone already in the steel casing which would also effect other aspects of the penetration process.

Overall we see that once the averaging range is calibrated, the model does a good job in reproducing the simulation results.

## A SHORT PARAMETER STUDY

The main material parameters that would effect the degree of confinement of ceramic targets are:

- spall strength $P_{min}$,
- zero pressure fracture strength $Y_o$,
- shear modulus G, and
- flow stress pressure dependence slope $\alpha_2$.

The effect of $P_{min}$ is shown in Fig. 10. The effects of the three other parameters are shown in Figs. 14, 15, and 16. We see that the effect of $Y_o$ and $\alpha_2$ is small and the effect of G is not large. The only parameter that may effect the degree of confinement significantly is therefore the tensile strength.

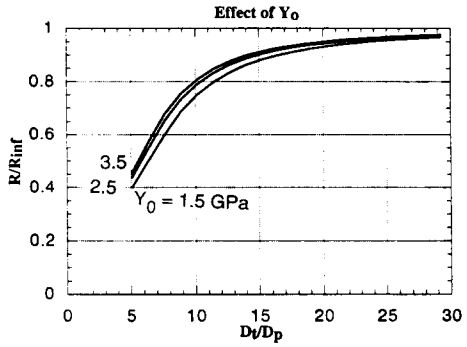


**Fig. 14. Effect of the initial (zero pressure) fracture strength.**

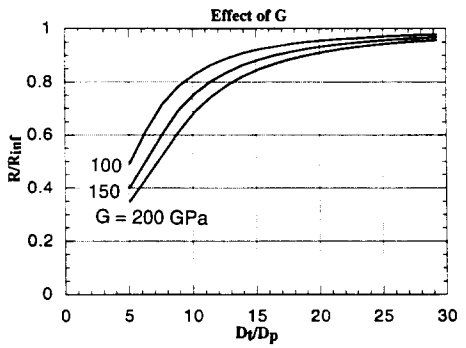


**Fig. 15. Effect of the shear modulus.**

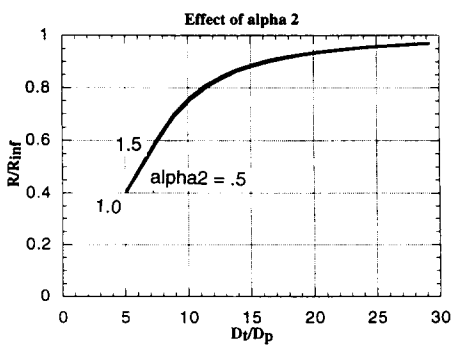


**Fig. 16. Effect of the slope ($\alpha_2$) in the pressure dependent flow stress.**

## SUMMARY AND CONCLUSIONS

We employ the quasistatic cavity expansion model to estimate the degree of reduction in resistance of ceramic targets, steel targets, and steel encased ceramic targets to long rod penetration.

Solving the cavity expansion problem for a laterally finite target, we conclude that the stress needed to continue opening the cavity ($\sigma_r$ (a)) is a decreasing function of the cavity radius "a." We determine the resistance R as an average over the range:

$$o \leq a \leq a_r \text{ where } a_r = \frac{1}{2} e\, D_P \text{ and } D_P \text{ is the projectile diameter.}$$

To validate the model and calibrate values for e, we ran 14 computer simulations using the CTH wavecode. Our main conclusions are:

- For ceramic (alumina) targets, e = 0.47 ± 0.02 represents quite well the simulation results at an impact velocity of 1.5 km/s.
- At a higher velocity (2.5 km/s) we get e ≅ 0.7. The averaging range ($a_r$ = ½ e $D_P$) increases with velocity which shows that the effectiveness of a given confinement decreases with velocity.
- For steel targets, the value of e is much higher. We get e ≅ 1.55 ± 0.15. Also, for the same diameter ratio, the effectiveness of a steel confinement is significantly higher than that of a ceramic confinement.
- Confining the ceramic in a steel casing increases the resistance, but not dramatically.
- The material parameter to which the degree of confinement of ceramic targets is most sensitive is the tensile strength (represented by the spall strength $P_{min}$). As $P_{min}$ is usually not well known for a specific ceramic material, significant uncertainties in estimating the degree of confinement may arise.
- Other material parameters (elastic moduli, compressive strength parameters) effect the degree of confinement only slightly.

## ACKNOWLEDGMENTS

This work was supported by the U.S. Army Armament Research, Development and Engineering Center (ARDEC) under contract DAAA21-90-D-0009.

## REFERENCES

1. Y. Partom and D. L. Littlefield, Dependence of ceramic armor resistance on projectile velocity. *Proc. 14th Int. Symp. on Ballistics*, **2**, 563-572, Quebec, Canada, July (1993).
2. Y. Partom, Efficiency of lateral self-confinement in metal and ceramic targets. IAT.R 0019, April (1993).
3. Y. Partom, Resistance ($R_t$) of ceramic targets confined in a steel casing. IAT.TN 0007, March (1993).
4. R. F. Bishop, R. Hill, and N. F. Mott, The theory of indentation and hardness tests. *Proc. Phys. Soc.*, **57**, 147-159 (1945).
5. J. M. McGlaun, et al., CTH: A three dimensional shock waves physics code. *Int. J. Impact Engng.*, **10**, 351-360 (1990).
6. Y. Partom and D. L. Littlefield, Validation of the cavity expansion resistance model for ceramic targets with computer simulations. IAT.R 0025, May (1993).
7. Y. Partom, Calibrating a strength model for AD995 alumina from plate impact VISAR profiles. IAT.R 0029, October (1993).